

Unsupervised Classification in Hyperspectral Imagery with Nonlocal Total Variation and Primal-Dual Hybrid Gradient Algorithm

Wei Zhu, Victoria Chayes, Alexandre Tiard, Stephanie Sanchez, Devin Dahlberg,
Andrea L. Bertozzi, Stanley Osher, Dominique Zosso, and Da Kuang

Abstract

In this paper, a graph-based nonlocal total variation method (NLTV) is proposed for unsupervised classification of hyperspectral images (HSI). The variational problem is solved by the primal-dual hybrid gradient (PDHG) algorithm. By squaring the labeling function and using a stable simplex clustering routine, an unsupervised clustering method with random initialization can be implemented. The effectiveness of this proposed algorithm is illustrated on both synthetic and real-world HSI, and numerical results show that the proposed algorithm outperforms other standard unsupervised clustering methods such as spherical K-means, nonnegative matrix factorization (NMF), and the graph-based Merriman-Bence-Osher (MBO) scheme.

Index Terms

Hyperspectral images (HSI), nonlocal total variation (NLTV), primal-dual hybrid gradient (PDHG) algorithm, unsupervised classification, stable simplex clustering

I. INTRODUCTION

HYPERSPECTRAL imagery (HSI) is an important domain in the field of remote sensing with numerous applications in agriculture, environmental science, mineralogy, and surveillance [1]. Hyperspectral sensors capture information of intensity of reflection at different wavelengths, from the infrared to ultraviolet. They take measurements 10-30nm apart, and up to 200 layers for a single image. Each pixel has a unique spectral signature, which can be used to differentiate objects that cannot be distinguished based on visible spectra, for example: invisible gas plumes, oil or chemical spills over water, or healthy from unhealthy crops.

The majority of HSI classification methods are either *unmixing* methods or *clustering* methods. Unmixing methods extract the information of the constitutive materials (the *endmembers*) and the abundance map [2]–[5]. Clustering methods do not extract endmembers; instead, they return the spectral signatures of the centroids of the clusters. Each centroid is the mean of the signatures of all the pixels in a cluster. However, when it is assumed that most of the pixels are dominated mostly by one endmember, i.e. in the absence of partial volume effects [6], which is usually the case for high-resolution HSI, these two types of methods are expected to give similar results [5]. The proposed nonlocal total variation (NLTV) method for HSI classification in this paper is a clustering method.

Much work has been carried out in the literature in both the unmixing and the clustering categories. HSI unmixing models can be characterized as linear or nonlinear. In a linear unmixing model (LUM), each pixel is approximated by a linear combination of the endmembers. When the linear coefficients are constrained to be nonnegative, it is equivalent to nonnegative matrix factorization (NMF), and good unsupervised classification results have been achieved in [3]–[5] using either NMF or hierarchical rank-2 NMF (H2NMF). Despite the simplicity of LUM, the assumption of a linear mixture of materials has been shown to be physically inaccurate in certain situations [7]. Researchers are starting to expand aggressively into the much more complicated nonlinear unmixing realm [8], where nonlinear effects such as atmospheric scattering are explicitly modeled. However, most of the work that has been done for nonlinear unmixing so far is supervised in the sense that prior knowledge of the endmember signatures is required [2]. Discriminative machine learning methods such as support vector machine (SVM) [9]–[11] and relevance vector machine (RVM) [12]–[14] based approaches have also been applied to hyperspectral images, but they are also supervised methods since a training set is needed to learn the classifiers.

On the contrary, graph-based clustering methods implicitly model the nonlinear mixture of the endmembers. This type of method is built upon a weight matrix that encodes the similarity between the pixels, which is typically a sparse matrix constructed using the distances between the spectral signatures. Graph-cut problems for graph segmentation have been well-studied in the literature [15]–[18]. In 2012, Bertozzi and Flenner proposed a diffuse interface model on graphs with applications

This work was supported by NSF grants DMS-1118971, DMS-1045536, DMS-1417674, and ONR grant N00014-16-1-2119
Wei Zhu, Da Kuang, Andrea L. Bertozzi, Stanley Osher, Dominique Zosso, and Stephanie Sanchez are with the Department of Mathematics at University of California, Los Angeles. Email: {weizhu731, dakuang, bertozzi, sjo, zosso}@math.ucla.edu, stephanie2000@g.ucla.edu
Victoria Chayes is with Bard College. Email: vminervachayes@gmail.com
Alexandre Tiard is with ENSE3, Grenoble Institute of Technology. Email: alexandretiard@gmail.com
Devin Dahlberg is with University of California, San Diego. Email: dahlbergdevin@gmail.com

to classification of high dimensional data [19]. This idea has been combined with the Merriman-Bence-Osher (MBO) scheme [20] and applied to multi-class graph segmentation [21], [22] and HSI classification [23], [24]. The method in [19] minimizes a graph version of the Ginzburg-Landau (GL) functional, which consists of the Dirichlet energy of the labeling function and a double-well potential, and uses Nyström extension to speed up the calculation of the eigenvectors for inverting the graph Laplacian. This graph-based method performed well compared to other algorithms in the detection of chemical plumes in hyperspectral video sequences [23], [24]. However, the GL functional is non-convex due to its double-well term, which may cause the algorithm to get stuck in local minima. This issue can be circumvented by running the algorithm multiple times with different initial conditions and hand-picking the best result.

The two methods proposed in this paper are unsupervised graph-based clustering techniques. Instead of minimizing the GL functional, which has been proved to converge to the total variation (TV) semi-norm, this work proposes to minimize the NLTV semi-norm of the labeling functions $\|\nabla_w u_l\|_{L^1}$ directly. A detailed explanation of the nonlocal operator ∇_w and the labeling function u_l will be provided in Section II and Section III. The L^1 regularized convex optimization problem is solved by the primal-dual hybrid gradient (PDHG) algorithm, which avoids the need to invert the graph Laplacian. We also introduce the novel idea of the quadratic model and a stable simplex clustering technique, which ensures that anomalies converge to their own clusters and makes random endmember initialization possible in the proposed algorithm. The direct usage of the NLTV semi-norm makes the proposed clustering methods more accurate than other methods when evaluated quantitatively on HSI with ground-truth labels, and the quadratic model with stable simplex clustering is a completely new addition to the field of HSI classification.

This paper is organized as follows: in Section II background is provided on total variation and nonlocal operators. Two NLTV models (linear and quadratic) and a stable simplex clustering method are presented in Section III. Section IV provides a detailed explanation on the application of the PDHG algorithm to solving the convex optimization problems in the linear and quadratic models. Section V presents the numerical results and a sensitivity analysis on the key model parameters. Section VI presents the conclusions.

II. TOTAL VARIATION AND NONLOCAL OPERATORS

Total variation (TV) method was introduced by Rudin et al in 1992 [25] and has been applied to various image processing tasks [26]. Its advantage is that one can preserve the edges in the image when minimizing $\|\nabla u\|_{L^1}$ (TV semi-norm). The total variation model is:

$$\min_u E(u) = \|\nabla u\|_{L^1} + \lambda S(u).$$

The parameter λ can be adjusted to give higher priority to the TV-regularizing term, or the data fidelity term $S(u)$.

Despite its huge success in image processing, the total variation method is still a local method. More specifically, the gradient of a pixel is calculated using its immediate adjacent pixels. It is known that local image processing techniques fail to produce satisfactory results when the image has repetitive structures, or intrinsically related objects in the image are not spatially connected. To address this problem, Buades et al proposed a nonlocal means method based on patch distances for image denoising [27]. Gilboa and Osher [28] later formalized a systematic framework for nonlocal image processing. Nonlocal image processing produces much better results because theoretically any pixel in the image can interact with any other, which better preserves texture and fine details.

In HSI classification, clusters can have elements that are not spatially connected. Thus it is necessary to develop a nonlocal method of gradient calculation. We provide a review of nonlocal operators in the rest of this section. Note that the model is continuous, and the weights are not necessarily symmetric [29].

Let Ω be a region in \mathbb{R}^n , and $u : \Omega \rightarrow \mathbb{R}$ be a real function. In the model for HSI classification, Ω is the domain of the pixels, and $u : \Omega \rightarrow [0, 1]$ is the labeling function of a cluster. The larger the value of $u(x)$, the more likely that pixel x would be classified in that cluster. The nonlocal derivative is:

$$\frac{\partial u}{\partial y}(x) := \frac{u(y) - u(x)}{d(x, y)}, \quad \text{for all } x, y \in \Omega,$$

where d is a positive distance between x and y . In the context of hyperspectral images, $d(x, y)$ provides a way to measure the similarity between pixels x and y . Smaller $d(x, y)$ implies more resemblance between these two pixels. The nonlocal weight is defined as $w(x, y) = d^{-2}(x, y)$.

The nonlocal gradient $\nabla_w u$ for $u \in L^2(\Omega)$ can be defined as the collection of all partial derivatives, which is a function from Ω to $L^2(\Omega)$, i.e. $\nabla_w u \in L^2(\Omega, L^2(\Omega))$:

$$\nabla_w u(x)(y) = \frac{\partial u}{\partial y}(x) = \sqrt{w(x, y)}(u(y) - u(x)).$$

The standard L^2 inner products on Hilbert spaces $L^2(\Omega)$ and $L^2(\Omega, L^2(\Omega))$ are used in the definition. More specifically, for $u_1, u_2 \in L^2(\Omega)$ and $v_1, v_2 \in L^2(\Omega, L^2(\Omega))$,

$$\begin{aligned}\langle u_1, u_2 \rangle &:= \int_{\Omega} u_1(x) u_2(x) dx, \\ \langle v_1, v_2 \rangle &:= \int_{\Omega} \int_{\Omega} v_1(x)(y) v_2(x)(y) dy dx.\end{aligned}$$

The nonlocal divergence div_w is defined as the negative adjoint of the nonlocal gradient:

$$\text{div}_w v(x) := \int_{\Omega} \sqrt{w(x, y)} v(x)(y) - \sqrt{w(y, x)} v(y)(x) dy.$$

At last, a standard L^1 and L^∞ norm is defined on the space $L^2(\Omega, L^2(\Omega))$:

$$\begin{aligned}\|v\|_{L^1} &:= \int_{\Omega} \|v(x)\|_{L^2} dx = \int_{\Omega} \left| \int_{\Omega} |v(x)(y)|^2 dy \right|^{\frac{1}{2}} dx, \\ \|v\|_{L^\infty} &:= \sup_x \|v(x)\|_{L^2}.\end{aligned}$$

III. TWO NLTV MODELS FOR UNSUPERVISED HSI CLASSIFICATION

In this section, two NLTV models are explained for unsupervised classification of HSI. The linear model runs faster in each iteration, but it requires a more accurate centroid initialization. The quadratic model runs slower in each iteration, but it is more robust with respect to the centroid initialization. Moreover, the quadratic model converges faster if the initialization is not ideal.

A. Linear Model

We extend the idea from [30] to formulate a linear model for classification on HSI. The linear model seeks to minimize:

$$\begin{aligned}E_1(u) &= \|\nabla_w u\|_{L^1} + \langle u, f \rangle \\ &= \sum_{l=1}^k \|\nabla_w u_l\|_{L^1} + \sum_{l=1}^k \int_{\Omega} u_l(x) f_l(x) dx,\end{aligned}\tag{1}$$

where $u = (u_1, u_2, \dots, u_k) : \Omega \rightarrow \mathbb{K}^k$ is the labeling function, k is the number of clusters, $\mathbb{K}^k = \{(x_1, x_2, \dots, x_k) | \sum_{i=1}^k x_i = 1, x_i \geq 0\}$ is the unit simplex in \mathbb{R}^k , and $\nabla_w u = (\nabla_w u_1, \dots, \nabla_w u_k)$ such that $\|\nabla_w u\|_{L^1} = \sum_{l=1}^k \|\nabla_w u_l\|_{L^1}$. $f_l(x)$ is the error function defined as $f_l(x) = \frac{\lambda}{2} |g(x) - c_l|_\mu^2$, where $g(x)$ and c_l are the spectral signatures of pixel x and the l -th centroid, which is initially either picked randomly from the HSI or generated by any fast unsupervised centroid extraction algorithm (e.g. H2NMF, K-means.) The distance in the definition of $f_l(x)$ is a linear combination of cosine distance and Euclidean distance:

$$|g(x) - c_l|_\mu = 1 - \frac{\langle g(x), c_l \rangle}{\|g(x)\|_2 \|c_l\|_2} + \mu \|g(x) - c_l\|_2, \quad \mu \geq 0.$$

In HSI processing, the cosine distance is generally used because it is more robust to atmospheric interference and topographical features [31]. The reason why the Euclidean distance is also used is that sometimes different classes have very similar spectral angles, but vastly different spectral amplitudes (e.g. “dirt” and “road” in the Urban dataset, which is illustrated in Section V.) This is called the linear model since the power of the labeling function u_l in (1) is one.

The intuition of the model is as follows: In order to minimize the fidelity term $\sum_{l=1}^k \int_{\Omega} u_l(x) f_l(x)$, a small $u_l(x)$ is required if $f_l(x)$ is large, while no such requirement is needed if $f_l(x)$ is relatively small. This combined with the fact that $(u_1(x), \dots, u_k(x))$ lies on a unit simplex implies that $u_l(x)$ would be the largest term if pixel x is mostly similar to the l -th centroid c_l . Meanwhile, the NLTV regularizing term $\sum_{l=1}^k \|\nabla_w u_l\|_{L^1}$ ensures that pixels similar to each other tend to have analogous values of u . Therefore a classification of pixel x can be obtained by choosing the index l that has the largest value $u_l(x)$.

Now we discuss how to discretize (1) for numerical implementation.

Algorithm 1 Linear Model

- 1: Initialization of centroids: Choose $(c_l)_{l=1}^k$ (randomized or generated by unsupervised centroid extraction algorithms).
 - 2: Initialization of parameters: Choose $\tau, \sigma > 0$ satisfying $\sigma\tau\|\nabla_w\|^2 \leq 1$, $\theta = 1$
 - 3: Initial iterate: Set $u^0 \in \mathbb{R}^{r \times k}$ and $p^0 \in \mathbb{R}^{(r \times r) \times k}$ randomly, set $\bar{u}^0 = u^0$, $u_{hard} = threshold(u^0)$
 - 4: **while** not converge **do**
 - 5: Minimize energy E_1 using PDHG algorithm
 - 6: $u_{hard} = threshold(u)$
 - 7: Update $(c_l)_{l=1}^k$
 - 8: **end while**
-

1) *Weight Matrix*: Following the idea from [28], the patch distance is defined as:

$$d_\sigma(x, y) = \int_{\Omega} G_\sigma(t) |g(x+t) - g(y+t)|^2 dt,$$

where G_σ is a Gaussian of standard deviation σ . To build a sparse weight matrix, we take a patch P_i around every pixel i , and truncate the weight matrix by constructing a k -d tree [32] and searching the m nearest neighbors of P_i . k -d tree is a space-partitioning data structure that can significantly reduce the time cost of nearest neighbor search [33]. We employ a randomized and approximate version of this algorithm [34] implemented in the open source VLFeat package¹. The weight is binarized by setting all nonzero entries to one. In the experiments, patches of size 3×3 are used, and m is set to 10. Note that unlike RGB image processing, the patch size for HSI does not have to be very large. The reason is that while low dimensional RGB images require spatial context to identify pixels, high dimensional hyperspectral images already encode enough information for each pixel in the spectral dimension. Of course, a larger patch size that is consistent with the spatial resolution of the HSI will still be preferable when significant noise is present.

2) *The Labeling Function and the Nonlocal Operators*: The labeling function, $u = (u_1, u_2, \dots, u_k)$, is discretized as a matrix of size $r \times k$, where r is the number of pixels in the hyperspectral image, and $(u_l)_j$ is the l -th labeling function at j -th pixel; $(\nabla_w u_l)_{i,j} = \sqrt{w_{i,j}}((u_l)_j - (u_l)_i)$ is the nonlocal gradient of u_l ; $(\text{div}_w v)_i = \sum_j \sqrt{w_{i,j}}v_{i,j} - \sqrt{w_{j,i}}v_{j,i}$ is the divergence of v at i -th pixel; and the discrete L^1 and L^∞ norm of $\nabla_w u_l$ are defined as: $\|\nabla_w u_l\|_{L^1} = \sum_i \left(\sum_j (\nabla_w u_l)_{i,j}^2 \right)^{\frac{1}{2}}$, and $\|\nabla_w u_l\|_{L^\infty} = \max_i \left(\sum_j (\nabla_w u_l)_{i,j}^2 \right)^{\frac{1}{2}}$.

The next issue to address is how to minimize (1) efficiently. The convexity of the energy functional E_1 allows us to consider using convex optimization methods. First-order primal-dual algorithms have been successfully used in image processing with L^1 type regularizers [30], [35]–[37]. We use the primal-dual hybrid gradient (PDHG) algorithm. The main advantage is that no matrix inversion is involved in the iterations, as opposed to general graph Laplacian methods. The most expensive part of the computation comes from sparse matrix multiplications, which are still inexpensive due to the fact that only $m = 10$ nonzero elements are kept in each row of the nonlocal weight matrix.

We then address centroid updates and stopping criteria for the linear model. The concept of centroid updates is not uncommon; in fact, the standard K-means algorithm consists of two steps: first, it assigns each point to a cluster whose mean yields the least within-cluster sum of squares, then it re-calculates the means from the centroids, and terminates when assignments no longer change [38]. Especially for data-based methods, re-calculating the centroid is essential for making the algorithm less sensitive to initial conditions and more likely to find the “true” clusters.

After solving (1) using the PDHG algorithm, the output u will be thresholded to u_{hard} . More specifically, for every $i \in \{1, 2, \dots, r\}$, the largest element among $((u_1)_i, (u_2)_i, \dots, (u_k)_i)$ is set to 1, while the others are set to 0, and we claim the i -th pixel belongs to that particular cluster. Then the l -th centroid is updated by taking the mean of all the pixels in that cluster. The process is repeated until the difference between two consecutive u_{hard} drops below a certain threshold. The pseudocode for the proposed linear model on HSI is listed in Algorithm 1.

Before ending the discussion of the proposed linear model, we point out its connection to the piecewise constant Mumford-Shah model for multi-class graph segmentation [39]. Assume that the domain Ω of the HSI is segmented by a contour Φ into k disjoint regions, $\Omega = \cup_{l=1}^k \Omega_l$. The piecewise constant Mumford-Shah energy is defined as:

$$E_{MS}(\Phi, \{c_l\}_{l=1}^k) = |\Phi| + \lambda \sum_{l=1}^k \int_{\Omega_l} |g(x) - c_l|^2 dx, \quad (2)$$

¹<http://www.vlfeat.org>

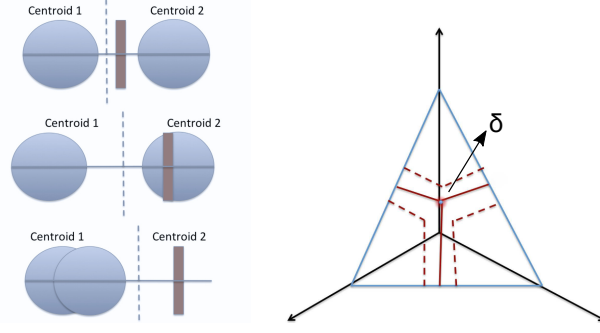


Fig. 1. The first figure shows the “pushing” mechanism of the quadratic model. The horizontal line represents the unit simplex in \mathbb{R}^2 . Signatures from cluster A_1 are colored blue, and signatures from cluster A_2 are colored brown. The vertical dashed bar is generated by a stable simplex clustering method, and it thresholds the points on the simplex into two categories.

The second figure shows the stable simplex clustering. Every grid point δ on the simplex generates a simplex clustering. We want to choose a δ such that there are very few data points falling into the “Y-shaped region”.

where $|\Phi|$ is the length of the contour. To illustrate the connection between (1) and (2), consider the “local” version of (1), which essentially replaces the NLTV regularizer $\|\nabla_w u_l\|_{L^1}$ with its local counterpart :

$$E_1^{\text{loc}}(u) = \sum_{l=1}^k \|\nabla u_l\|_{L^1} + \sum_{l=1}^k \int u_l(x) f_l(x) dx. \quad (3)$$

Assume that the labeling function u_l is the characteristic function of Ω_l . Then $\int u_l(x) f_l(x) dx$ is equal to $\int_{\Omega_l} |g(x) - c_l|^2 dx$ up to a multiplicative constant. Moreover, the total variation of a characteristic function of a region equals the length of its boundary, and hence $|\Phi| = \sum_{l=1}^k \|\nabla u_l\|_{L^1}$. So the linear model (1) can be viewed as a nonlocal convex-relaxed version of Mumford-Shah model. We also note that the linear energy (1) has been studied in [23]. But in their work, the authors used a graph-based MBO method to minimize (1) instead of the PDHG algorithm, and the difference of the numerical performances can be seen in Section V.

B. Quadratic Model

1) *Intuition:* The aforementioned linear model performs very well when the centroids are initialized by accurate centroid extraction algorithms. As shown in Section V, the linear model can have a significant boost to the accuracy of other algorithms if the centroid extraction algorithm is reasonable, without sacrificing speed. However, if centroids are not extracted accurately, or if random initialization is used, the segmenting results are no longer reliable, and the algorithm takes far more iterations to converge to a stable classification.

To reduce the times of centroid updates and merge similar clusters automatically and simultaneously, the following quadratic model is proposed:

$$E_2(u) = \sum_{l=1}^k \|\nabla_w u_l\|_{L^1} + \sum_{l=1}^k \int u_l^2(x) f_l(x) dx. \quad (4)$$

Similar as before, $u = (u_1, u_2, \dots, u_k) : \Omega \rightarrow \mathbb{K}^k$ is the labeling function, k is the number of clusters, \mathbb{K}^k is the unit simplex in \mathbb{R}^k , and $f_l(x)$ is the error function.

Note that the only difference between (1) and (4) is that the power of the labeling function u_l here is two. The intuition for this is as follows:

Consider for simplicity a hyperspectral image with a ground truth of only two clusters, A_1 and A_2 . Suppose the randomized initial centroids are chosen such that $c_1 \approx c_2 \in A_1$; or, that the two random initial pixels are of very similar spectral signatures and belong to the same ground truth cluster.

Let x be a pixel from A_2 . Then $0 \ll |g(x) - c_1|^2 \approx |g(x) - c_2|^2$. When (1) is applied, the fidelity term $\langle u, f \rangle$ does not change when $u(x)$ moves on the simplex in \mathbb{R}^2 , and thus pixels of A_2 will be scattered randomly on the simplex. After thresholding, an approximately equal number of pixels from cluster A_2 will belong to clusters C_1 and C_2 , so the new centroids \tilde{c}_1 and \tilde{c}_2 that are the means of the spectral signatures of the current clusters will once again be approximately equal.

This situation changes dramatically when (4) is minimized:

- Observe that the fidelity term in E_2 is minimized for a pixel $x \in A_2$ when $u_1(x) \approx u_2(x) \approx \frac{1}{2}$. Therefore, the pixels of cluster A_2 will be “pushed” toward the center of the simplex once E_2 is minimized.
- With a stable simplex clustering method (explained in Section III-B2), the clusters are divided such that all of these pixels in the center belong to either C_1 or C_2 ; without loss of generality suppose they belong to C_2 . Then the updated centroid

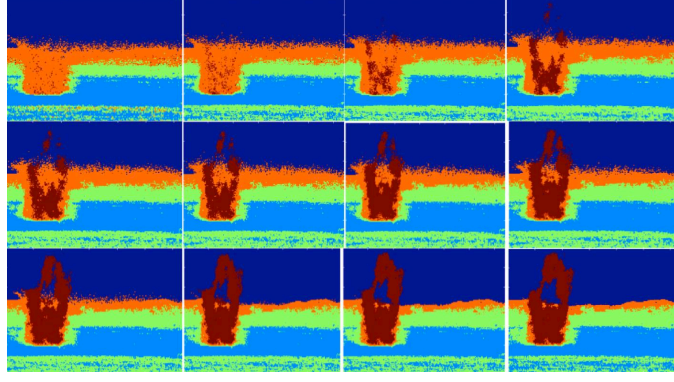


Fig. 2. Quadratic model and stable simplex clustering on the plume dataset. The chemical plume (brown) is perfectly detected in 12 iterations.

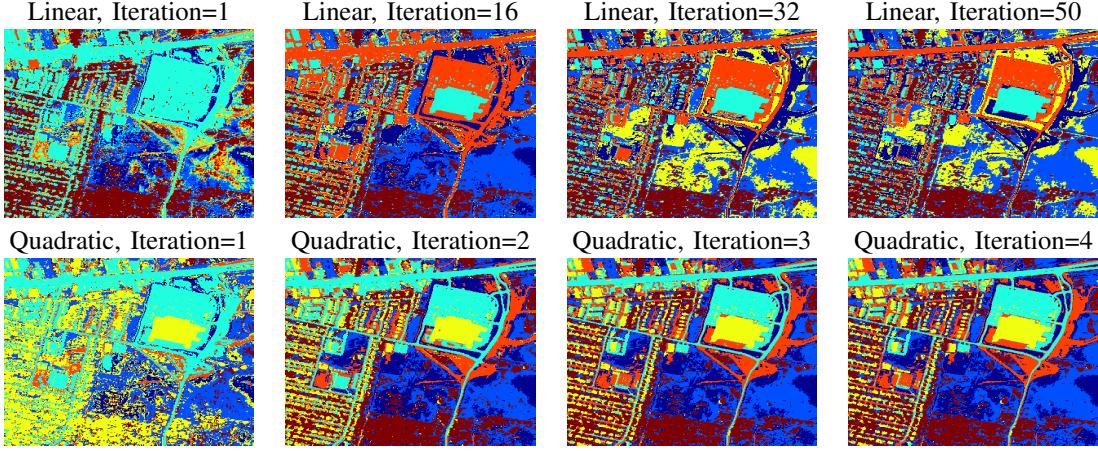


Fig. 3. Linear vs Quadratic Model on the Urban dataset with the same centroid initialization. To produce essentially identical results, the Linear model (first row) took 50 iterations of centroid updates, and the Quadratic model (second row) took just 4 iterations.

\tilde{c}_1 is essentially c_1 , while the updated centroid \tilde{c}_2 is a linear combination of the spectral signature of members belonging to A_1 and A_2 , and thus quite different from the original c_2 .

- After minimizing the energy E_2 again, pixels from A_1 will be clustered in C_1 , and pixels from A_2 will be pushed to C_2 . Therefore, the clustering will be finished in just two steps in theory. See Fig.1 for a graphical illustration.

The quadratic model not only reduces the number of iterations needed to find the “true” clustering because of its capability of anomaly detection, but it allows for random initialization as well, making it a more robust technique.

2) *Stable Simplex Clustering*: As mentioned above, the quadratic model pushes anomalies into the middle of the unit simplex. Therefore it would be ill-conceived to simply classify the pixels based on the largest component of the labeling function $u(x) = (u_1(x), u_2(x), \dots, u_k(x))$. Instead, a stable simplex clustering method has to be used.

The concept behind the stable simplex clustering is to choose a division that puts all the data points in the “middle” of the unit simplex into a single cluster. Fig. 1 demonstrates this in the simple two-cluster case. Also refer to section III-B1 for explanation of the “pushing” process. The idea to accomplish this goal is inspired by [5]. We first create a grid on a k -dimensional simplex, where k is the number of clusters, and each grid point δ generates a simplex clustering. Then a δ is searched to minimize the energy $g(\delta)$:

$$g(\delta) = -\log\left(\prod_{l=1}^k F_l(\delta)\right) + \eta \exp(G(\delta)),$$

where $F_l(\delta)$ is the percentage of data points in cluster l , and $G(\delta)$ is the percentage of data points on the edges near the division, i.e. the “Y-shaped region” in Figure 1. The first term in $g(\delta)$ rewards keeping clusters approximately of the same size, ensuring no skewed data from clusters far too small. And the second term rewards sparsity of points in the intermediate region. The constant η is chosen to be large enough such that stability has a bigger weight in the energy.

Algorithm 2 shows the quadratic model using stable simplex clustering. Fig. 2 demonstrates how this detected the chemical plumes in a frame with background centroids pre-calculated and random initialization for the final centroid. Notice that no plume is detected in the first iteration. But by the twelfth iteration, the gas plume is nearly perfectly segmented.

Algorithm 2 Quadratic Model with Stable Simplex Clustering

- 1: Initialization of centroids: Choose $(c_l)_{l=1}^k$ (randomized or generated by unsupervised centroid extraction algorithms).
 - 2: Initialization of parameters: Choose $\tau, \sigma > 0$ satisfying $\sigma\tau\|\nabla_w\|^2 \leq 1$, $\theta = 1$
 - 3: Initial iterate: Set $u^0 \in \mathbb{R}^{r \times k}$ and $p^0 \in \mathbb{R}^{(r \times r) \times k}$ randomly, set $\bar{u}^0 = u^0$,
 - 4: **while** not converge **do**
 - 5: Minimize energy E_2 using PDHG algorithm
 - 6: $u_{hard} = \text{threshold}(u)$ with stable simplex clustering
 - 7: Update $(c_l)_{l=1}^k$
 - 8: **end while**
-

Algorithm 3 Primal-Dual Hybrid Gradient (PDHG) Algorithm

- 1: Initialization: Choose $\tau, \sigma > 0$, $\theta \in [0, 1]$, $(x^0, y^0) \in X \times Y$, and set $\bar{x}^0 = x^0$
 - 2: **while** not converge **do**
 - 3: $y^{n+1} = (I + \sigma\partial F^*)^{-1}(y^n + \sigma K\bar{x}^n)$
 - 4: $x^{n+1} = (I + \tau\partial G)^{-1}(x^n - \tau K^*y^{n+1})$
 - 5: $\bar{x}^{n+1} = x^{n+1} + \theta(x^{n+1} - x^n)$
 - 6: $n = n + 1$
 - 7: **end while**
-

Finally, we present the comparison between the results of the linear model and the quadratic model on the Urban dataset with identical random pixel initialization in Figure 3. The linear model took about 50 iterations to converge, and the quadratic model only took 4 iterations.

IV. PRIMAL-DUAL HYBRID GRADIENT ALGORITHM

In this section, a detailed explanation is provided on the application of the PDHG algorithm [30], [35]–[37] to minimizing E_1 (1) and E_2 (4) in the previous section. A review of the algorithm is provided in a more general setting to contextualize the extension to nonlocal model for hyperspectral imagery.

A. A Review of PDHG Algorithm

Consider the following convex optimization problem:

$$\min_{x \in X} \{F(Kx) + G(x)\}, \quad (5)$$

where X and Y are finite-dimensional real vector spaces, F and G are proper convex lower semi-continuous functions $F : Y \rightarrow [0, \infty]$, $G : X \rightarrow [0, \infty]$, and $K : X \rightarrow Y$ is a continuous linear operator with the operator norm $\|K\| = \sup\{\|Kx\| : x \in X, \|x\| \leq 1\}$. The primal-dual formulation of (5) is the saddle-point problem:

$$\min_{x \in X} \max_{y \in Y} \{\langle Kx, y \rangle - F^*(y) + G(x)\}, \quad (6)$$

where F^* is the convex conjugate of F defined as $F^*(y) = \sup_x \langle x, y \rangle - F(x)$

The saddle-point problem (6) is then solved using the iterations of Algorithm 3 from [30].

In Algorithm 3, $(I + \lambda\partial f)^{-1}(x)$ is the proximal operator of f , which is defined as:

$$(I + \lambda\partial f)^{-1}(x) = \text{prox}_{\lambda f}(x) = \arg \min_y f(y) + \frac{1}{2\lambda}\|y - x\|_2^2.$$

It has been shown in [30] that $O(1/N)$ (where N is the number of iterations) convergence can be achieved as long as σ, τ satisfy $\sigma\tau\|K\|^2 \leq 1$.

B. Primal-Dual Iterations to Minimize E_1 and E_2

Recall from Section III that the discretized linear and quadratic energy E_1 and E_2 are:

$$\begin{aligned} E_1(u) &= \sum_{l=1}^k \|\nabla_w u_l\|_{L^1} + \sum_{l=1}^k \sum_{i=1}^r (u_l)_i (f_l)_i, \\ &= \|\nabla_w u\|_{L^1} + \langle u, f \rangle, \\ E_2(u) &= \sum_{l=1}^k \|\nabla_w u_l\|_{L^1} + \sum_{l=1}^k \sum_{i=1}^r (u_l)_i^2 (f_l)_i, \\ &= \|\nabla_w u\|_{L^1} + \langle u, f \odot u \rangle, \end{aligned}$$

Algorithm 4 Primal-Dual Iterations for the Linear Model

```

1: while not converge do
2:    $p^{n+1} = \text{proj}_P(p^n + \sigma \nabla_w \bar{u}^n)$ 
3:    $u^{n+1} = \text{proj}_U(u^n + \tau \text{div}_w p^{n+1} - \tau f)$ 
4:    $\bar{u}^{n+1} = u^{n+1} + \theta(u^{n+1} - u^n)$ 
5:    $n = n + 1$ 
6: end while

```

Algorithm 5 Primal-Dual Iterations for the Quadratic Model

```

1: while not converge do
2:    $p^{n+1} = \text{proj}_P(p^n + \sigma \nabla_w \bar{u}^n)$ 
3:   Update  $u^{n+1}$  as in (12), where  $\tilde{u} = u^n + \tau \text{div}_w p^{n+1}$ 
4:    $\bar{u}^{n+1} = u^{n+1} + \theta(u^{n+1} - u^n)$ 
5:    $n = n + 1$ 
6: end while

```

where $u = (u_1, u_2, \dots, u_k)$ is a nonnegative matrix of size $r \times k$, with each row of matrix u summing to one, and $f \odot u$ denotes the pointwise product between two matrices f and u . After adding an indicator function δ_U , minimizing E_1 and E_2 are equivalent to solving (7) and (8):

$$\min_u \|\nabla_w u\|_{L^1} + \langle u, f \rangle + \delta_U(u), \quad (7)$$

$$\min_u \|\nabla_w u\|_{L^1} + \langle u, f \odot u \rangle + \delta_U(u) \quad (8)$$

where $U = \{u = (u_1, u_2, \dots, u_k) \in \mathbb{R}^{r \times k} : \sum_{l=1}^k (u_l)_i = 1, \forall i = 1, \dots, r, (u_l)_i \geq 0\}$, and δ_U is the indicator function on U . More specifically:

$$\delta_U(u) = \begin{cases} 0 & \text{if } u \in U, \\ \infty & \text{otherwise.} \end{cases} \quad (9)$$

By comparing (7), (8) and (5), we can set $K_1 = K_2 = \nabla_w$, $F_1(q) = F_2(q) = \|q\|_{L^1}$, $G_1(u) = \langle u, f \rangle + \delta_U(u)$, and $G_2(u) = \langle u, f \odot u \rangle + \delta_U(u)$. The convex conjugate of F_1 (and F_2) is $F_1^*(p) = F_2^*(p) = \delta_P(p)$, where the set $P = \{p \in \mathbb{R}^{(r \times r) \times k} : \|p_l\|_\infty \leq 1\}$.

Next, we derive the closed forms of the proximal operators $(I + \sigma \partial F_{1,2}^*)^{-1}$ and $(I + \tau \partial G_{1,2})^{-1}$ so that Algorithm 3 can be implemented efficiently to minimize E_1 and E_2 .

$$\begin{aligned} (I + \sigma \partial F_{1,2}^*)^{-1}(\tilde{p}) &= (I + \sigma \partial \delta_P)^{-1}(\tilde{p}) \\ &= \arg \min_p \delta_P(p) + \frac{1}{2\sigma} \|p - \tilde{p}\|_2^2 = \text{proj}_P(\tilde{p}), \end{aligned} \quad (10)$$

where $\text{proj}_P(\tilde{p})$ is the projection of \tilde{p} onto the closed convex set P .

$$\begin{aligned} (I + \tau \partial G_1)^{-1}(\tilde{u}) &= \arg \min_u \langle u, f \rangle + \delta_U(u) + \frac{1}{2\tau} \|u - \tilde{u}\|_2^2 \\ &= \arg \min_{u \in U} \|u - \tilde{u} + \tau f\|_2^2 = \text{proj}_U(\tilde{u} - \tau f). \end{aligned} \quad (11)$$

$$\begin{aligned} (I + \tau \partial G_2)^{-1}(\tilde{u}) &= \arg \min_u \left\langle u, \frac{\tau}{2} \mathcal{A}u \right\rangle + \tau \delta_U(u) + \frac{1}{2} \|u - \tilde{u}\|_2^2 \\ &= \arg \min_{u \in U} \frac{1}{2} \langle u, (I + \tau \mathcal{A})u \rangle - \langle u, \tilde{u} \rangle + \frac{1}{2} \langle \tilde{u}, (I + \tau \mathcal{A})^{-1} \tilde{u} \rangle \\ &= \arg \min_{u \in U} \frac{1}{2} \|(I + \tau \mathcal{A})^{\frac{1}{2}} u - (I + \tau \mathcal{A})^{-\frac{1}{2}} \tilde{u}\|_2^2, \end{aligned} \quad (12)$$

where $\mathcal{A} : \mathbb{R}^{r \times k} \rightarrow \mathbb{R}^{r \times k}$ is a linear operator defined as $\frac{1}{2} \mathcal{A}u = f \odot u$. Therefore \mathcal{A} is a positive semidefinite diagonal matrix of size $rk \times rk$. It is worth mentioning that the matrix $(I + \tau \mathcal{A})$ is diagonal and positive definite, and hence it is trivial to compute its inverse and square root. Problem (12) can be solved as a preconditioned projection onto the unit simplex \mathbb{K}^k , and the solution will be explained in Section IV-C.

Combining (10,11,12) and Algorithm 3, we have the primal-dual iterations for minimizing E_1 (Algorithm 4) and E_2 (Algorithm 5).

Before moving on to explaining how to solve (12), we specify the two orthogonal projections proj_P and proj_U in Algorithm 4: Let $\tilde{p} = \text{proj}_P(p)$, where $p = (p_l)_{l=1}^k \in \mathbb{R}^{(r \times r) \times k}$. Then for every $i \in \{1, 2, \dots, r\}$ and every $l \in \{1, 2, \dots, k\}$, the i -th row

of \tilde{p}_i is the projection of the i -th row of p_l on to the unit ball in \mathbb{R}^r . Similarly, if $\tilde{u} = \text{proj}_U(u)$, then for every $i \in \{1, 2, \dots, r\}$, $((\tilde{u}_1)_i, (\tilde{u}_2)_i, \dots, (\tilde{u}_k)_i)$ is the projection of $((u_1)_i, (u_2)_i, \dots, (u_k)_i)$ onto the unit simplex \mathbb{K}^k in \mathbb{R}^k .

C. Preconditioned Projection onto the Unit Simplex

This section is dedicated to solving (12). It is easy to see that the rows of u in (12) are decoupled, and the only problem that needs to be solved is:

$$\min_{u \in \mathbb{R}^k} \delta_{\mathbb{K}^k}(u) + \frac{1}{2} \|Au - y\|^2, \quad (13)$$

where $A = \text{diag}(a_1, a_2, \dots, a_k)$ is a positive definite diagonal matrix of size $k \times k$, \mathbb{K}^k is the unit simplex in \mathbb{R}^k , and $y \in \mathbb{R}^k$ is a given vector.

Theorem 1: The solution $u = (u_1, u_2, \dots, u_k)$ of (13) is:

$$u_i = \max \left(\frac{a_i y_i - \lambda}{a_i^2}, 0 \right), \quad (14)$$

where λ is the unique number satisfying:

$$\sum_{i=1}^k \max \left(\frac{a_i y_i - \lambda}{a_i^2}, 0 \right) = 1 \quad (15)$$

The proof of Theorem 1 is shown in the Appendix. The most computationally expensive part of solving (15) is sorting the sequence $(a_i y_i)_{1 \leq i \leq k}$ of length k , which is trivial since k , the number of clusters, is typically a small number.

V. NUMERICAL RESULTS

A. Comparison Methods and Experimental Setup

All experiments were run on a Linux machine with Intel core i5, 3.3Hz with 2GB of DDR3 RAM. The following unsupervised algorithms have been tested:

- 1) **(Spherical) K-means:** Built in MatLab Code.
- 2) **NMF:** Non-negative Matrix Factorization [40].
- 3) **H2NMF:** Hierarchical Rank-2 Non-negative Matrix Factorization [5].
- 4) **MBO:** Graph Merriman-Bence-Osher scheme [23], [24]. The code is run for 10 times on each dataset, and the best result is chosen.
- 5) **NLTV2:** Nonlocal Total Variation, quadratic model with random pixel initialization.
- 6) **NLTV1(H2NMF/K-means):** Nonlocal Total Variation, linear model with endmembers/centroids extracted from H2NMF/K-means.

Every algorithm can be initialized via the same procedure as that in “K-means++” [41], and the name “Algorithm++” is used if the algorithm is initialized in such a way. For example, “NLTV2++” means nonlocal total variation, quadratic model with “K-means++” initialization procedure.

The algorithms are compared on the following datasets:

- 1) **Synthetic Dataset:** This dataset² contains five endmembers and 162 spectral bands. The 40,000 abundance vectors were generated as a sum of Gaussian fields. The dataset was generated using a Generalized Bilinear Mixing Model (GBM):

$$y = \sum_{i=1}^p a_i e_i + \sum_{i=1}^{p-1} \sum_{j=i+1}^p \gamma_{ij} a_i a_j e_i \odot e_j + n,$$

where γ_{ij} are chosen uniformly and randomly in the interval $[0, 1]$, n is the Gaussian noise, with an SNR of 30 dB, and a_i satisfies: $a_i \geq 0$, and $\sum_{i=1}^p a_i = 1$.

- 2) **Salinas-A Dataset:** Salinas-A scene³ was a small subscene of Salinas image, which was acquired by the AVIRIS sensor over Salinas Valley. It contains 86×83 pixels and 204 bands. The ground truth includes six classes: broccoli, corn, and four types of lettuce.
- 3) **Urban Dataset:** The Urban dataset⁴ is from HYperspectral Digital Imagery Collection Experiment (HYDICE), which has 307×307 pixels and contains 162 clean spectral bands. This dataset only has six classes of material: road, dirt, house, metal, tree, and grass.

²Available at <http://www.math.ucla.edu/~weizhu731/>

³Available at http://www.ehu.es/ccwintco/index.php?title=Hyperspectral_Remote_Sensing_Scenes

⁴Available at <http://www.agc.army.mil/>.

TABLE I
KEY PARAMETERS USED FOR DIFFERENT DATASETS

Datasets	λ	μ	Datasets	λ	μ
Synthetic	10^{-1}	10^{-4}	Plume	10^7	10^{-2}
Urban	10^6	10^{-5}	Pavia	10^6	10^{-8}
Salinas-A	10^4	10^{-4}	Pines	10^6	10^{-9}
SDA	10^6	10^{-7}	KSC	10^6	10^{-8}

TABLE II
COMPARISON OF NUMERICAL RESULTS ON THE SYNTHETIC AND SALINAS-A DATASETS

Algorithm	Synthetic		Salinas-A	
	Run-Time	Accuracy	Run-Time	Accuracy
K-means++	2s	90.98%	0.9s	79.92%
NMF++	9s	80.99%	1.0s	64.47%
H2NMF	2s	72.02%	1.5s	70.08%
MBO++	21s	84.49%	7.8s	68.62%
NLTV2++	29s	99.93%	1.6s	83.69%
NLTV1(K-means)	29s	95.96%	3.4s	83.75%

- 4) **San Diego Airport Dataset:** The San Diego Airport (SDA) dataset⁵ is provided by the HYDICE sensor. It comprises 400×400 pixels and contains 158 clean spectral bands. There are seven types of material: trees, grass, three types of road surfaces, and two types of rooftops [5]. The RGB image with cluster labels are shown in Fig. 7.
- 5) **Chemical Plume Dataset:** The chemical plume dataset⁶ consists of frames taken from a hyperspectral video of the release of chemical plumes provided by the John Hopkins University Applied Physics Laboratory. The image has 128×320 pixels, with 129 clean spectral bands. There was no ground truth provided for this data, so a segmentation of four classes is assumed: chemical plume, sky, foreground, and mountain. A fifth cluster is added so that the noise pixels would not interfere with the segmentation [23].
- 6) **Pavia University Dataset:** The Pavia University dataset is collected by the ROSIS sensor. It contains 103 clean spectral bands and 610×340 pixels, and comprises 9 classes of material.
- 7) **Indian Pines Dataset:** The Indian Pines dataset was acquired by AVIRIS sensor and consists of 145×145 pixels, with 200 clean spectral bands. The available ground truth is labeled into 16 classes.
- 8) **Kennedy Space Center Dataset:** This dataset was gathered by the NASA AVIRIS sensor over the Kennedy Space Center, Florida. A subscene of the western shore of the center is used in the numerical experiment. 12 classes of different materials are reported in the datacube of size $512 \times 365 \times 176$.

K-means and NMF are non-parametric, and the parameter setups of H2NMF and the MBO scheme are described in [5] and [23], [24]. The key parameters λ and μ in the NLTV models are determined in the following way:

- 1) λ is chosen such that the data fidelity term is around 10 times larger than the NLTV regularizing term $\|\nabla_w u\|_{L^1}$.
- 2) μ is chosen such that the Euclidean distances between different endmembers are roughly 10 times smaller than the cosine distances.

Table I displays the parameters chosen for the numerical experiments. The large variance of the parameter scales results from the variety of image sizes and scales. A sensitivity analysis over the parameters is presented in Section V-G.

B. Synthetic Dataset and Salinas-A Dataset

All the algorithms are first tested on the synthetic dataset. The classification results are shown in Table II and Fig. 4. Both NLTV algorithms have better overall accuracy than all of the other methods, although they took a longer time to converge. The quadratic model classified the image almost perfectly.

The visual classification results and overall accuracies of the Salinas-A dataset are shown in Fig. 5 and Table II. Both NLTV methods performed at higher accuracy compared to other methods. The linear model improved the result of K-means by incorporating spatial information of the dataset, and the quadratic model only took 4 iterations to converge.

C. Urban DataSet

There was no ground-truth provided for the Urban HSI. A structured sparse algorithm [42] (which is different from all of the testing algorithms) has been used to initialize a ground truth, which is then corrected pixel by pixel to provide a framework for

⁵Available at <http://www.math.ucla.edu/~weizhu731/>

⁶Available at <http://www.math.ucla.edu/~weizhu731/>

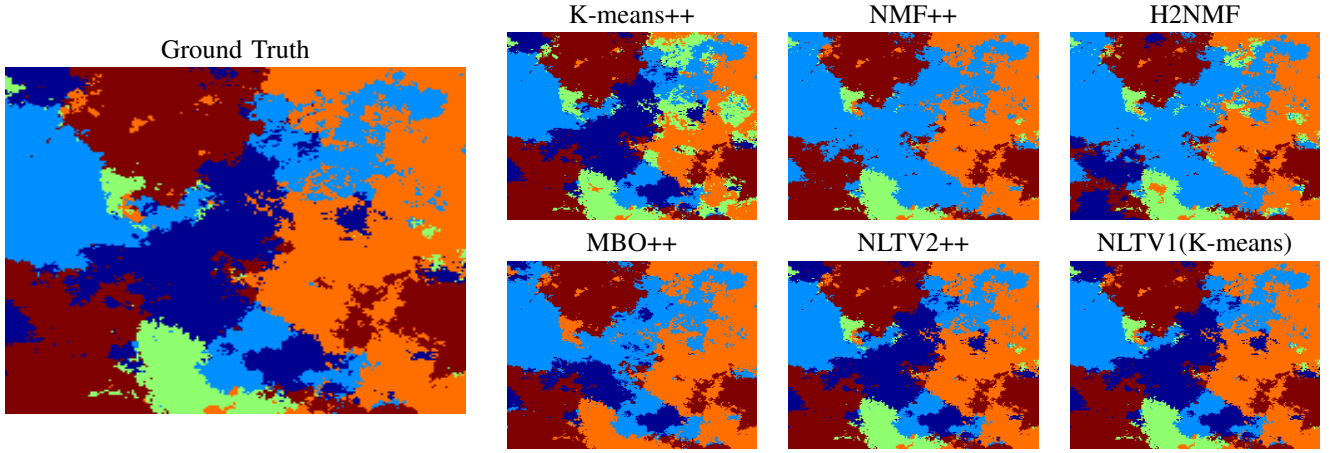


Fig. 4. Clustering results for the synthetic dataset generated by 5 endmembers. The first image on the left is the ground truth, and the remaining six images are the clustering results of the corresponding algorithms.

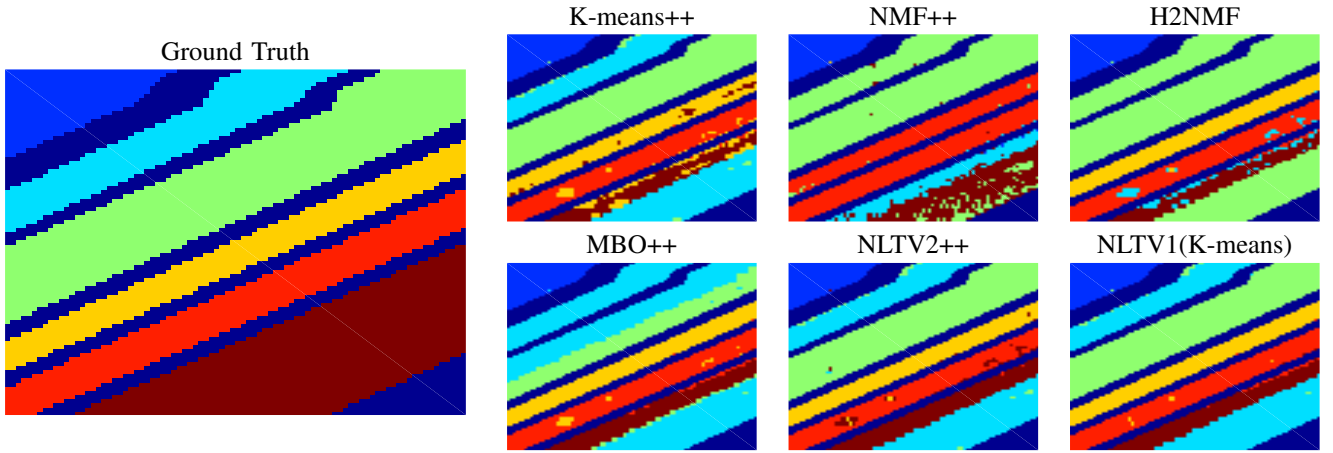


Fig. 5. Clustering results for the Salina-A dataset. The first image on the left is the ground truth, and the remaining six images are the clustering results of the corresponding algorithms.

TABLE III
COMPARISON OF NUMERICAL RESULTS ON THE URBAN DATASET

Algorithm	Run-Time	Accuracy
K-means	7s	75.20%
NMF	87s	55.70%
H2NMF	7s	85.96%
MBO	92s	78.86%
NLTV2	96s	92.14%
NLTV1(H2NMF)	17s	91.56%

numerical analysis of accuracy. As this “ground truth” was hand-corrected, it does not necessarily represent the most accurate segmentation of the image; however, it provides a basis for quantitative comparison.

After running all the algorithms that are compared to create six clusters, we noticed that they all split “grass” into two different clusters (one of them corresponds to a mixture of grass and dirt), while treating “road” and “metal” as the same. To obtain a reliable overall accuracy of the classification results, the two “grass” clusters are combined in every algorithm, hence obtaining the classification results for 5 clusters, which are “grass”, “dirt”, “road+metal”, “roof”, and “tree”.

The overall classification accuracies and run-times are displayed in Table III. As can be seen, the proposed NLTV algorithms performed consistently better with comparable run-time. It is easier to see visually in Fig. 6 that the NLTV algorithm performed best of the five algorithms tested; specifically, the NLTV algorithm alone distinguished all of the dirt beneath the parking lot and the intricacies of the road around the parking lot. The total variation regularizer also gives the segmented image smoother and more distinct edges, allowing easier human identification of the clusters.

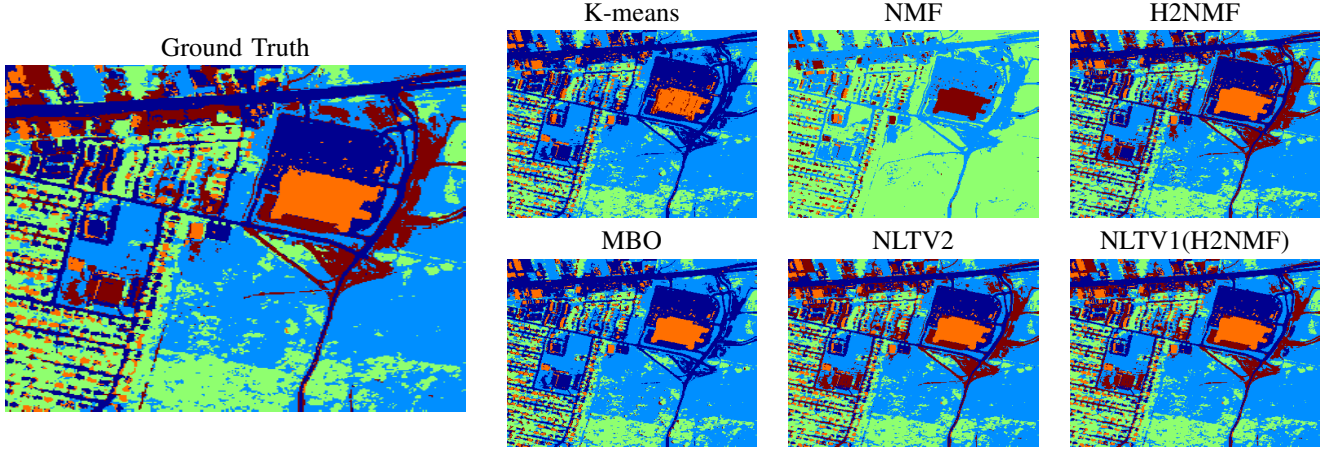


Fig. 6. Clustering results for the Urban dataset. Five clusters including rooftops, grass, trees, dirt, and “road+metal” are generated by the algorithms.

TABLE IV
RUN-TIMES FOR THE SAN DIEGO AIRPORT (SDA), CHEMICAL PLUME (PLUME), PAVIA UNIVERSITY (PAVIA), INDIAN PINES (PINES), AND KENNEDY SPACE CENTER (KSC) DATASETS

Algorithm	SDA	Plume	Pavia	Pines	KSC
K-means	9s	2s	26s	10s	47s
NMF	4s	2s	120s	19s	135s
H2NMF	13s	2s	12s	4s	24s
MBO	329s	18s	1020s	198s	754s
NLTV2	43s	23s	299s	64s	561s
NLTV1(H2NMF)	17s	18s	132s	21s	188s

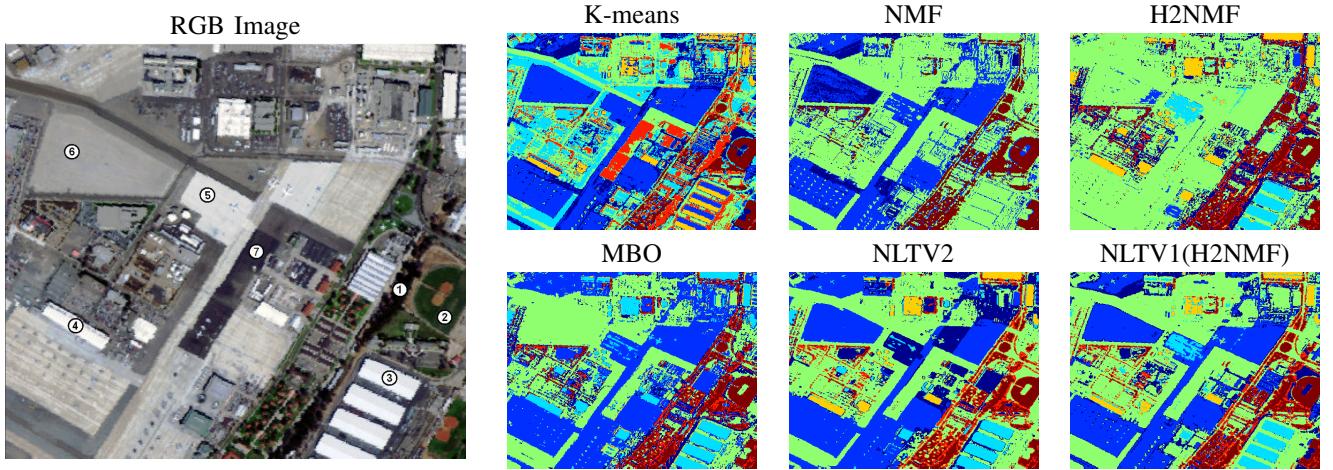


Fig. 7. Clustering results for the San Diego Airport dataset. The first image on the left is the RGB image, and the remaining six images are the clustering results of the corresponding algorithms.

D. San Diego Airport Dataset

The classification results and computational run-times are shown in Fig. 7 and Table IV. No ground truth classification is available for this HSI, but after examining the spectral signatures of various pixels in the scene, we managed to pinpoint some errors that were common for each algorithm. We will not go into detail about the NMF and H2NMF algorithms, which clearly do not perform well on this dataset. K-means obtained some decent results, but splitted the rooftops of the four buildings on the bottom right of the image into two distinct clusters, and failed to separate two different road types (cluster 5 and 6). The MBO scheme failed on two accounts: it did not properly segment two different road surfaces (cluster 6 and 7), and did not account for the different rooftop types (cluster 3 and 4). The linear NLTV model with H2NMF initialization is significantly more accurate than H2NMF and MBO. It successfully picked out two different types of roof (cluster 3 and 4), two different types of road (cluster 6 and 7), although the other type of road (cluster 5) is mixed with one type of roof (cluster 3). The best result was obtained by using the NLTV quadratic model with random initialization, with the only problem that tree and grass

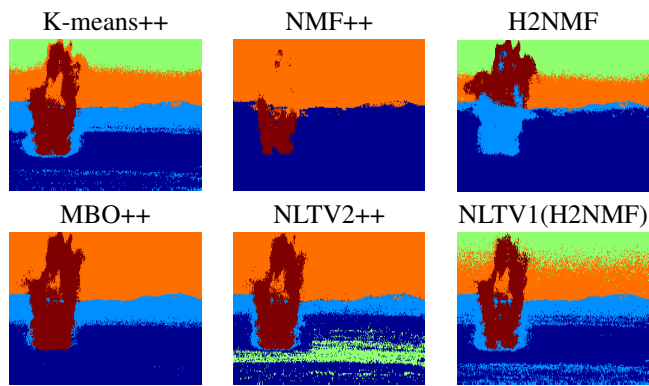


Fig. 8. Clustering results for the Chemical Plume dataset.

TABLE V
COMPARISON OF OVERALL ACCURACIES ON THE PAVIA UNIVERSITY, INDIAN PINES, AND KENNEDY SPACE CENTER DATASETS

Algorithm	Pavia	Pines	KSC
K-means++	42.31%	38.99%	41.73%
NMF++	54.97%	38.84%	37.07%
H2NMF	43.75%	36.78%	37.07%
MBO++	50.04%	36.49%	41.85%
NLTV, H2NMF init	42.83%	36.22%	41.41%
NLTV++	44.01%	42.35%	41.48%

(clusters 1 and 2) are mixed together. However, the mixing of grass and tree is actually the case for all the other algorithms. This means that NLTV quadratic model alone was able to identify six of the seven clusters correctly.

E. Chemical Plume Dataset

Analyzing images for chemical plumes is more difficult because of its diffusive nature. All the algorithms are run on the image before it was denoised and the results are shown in Figure 8. The unmixing methods such as NMF and H2NMF do not perform satisfactorily on this dataset. MBO++, K-means++, and NLTV2++ can all properly identify the chemical plume. Note that NLTV with H2NMF as centroid initialization outperforms H2NMF as a classification method. We have to point out that the NLTV quadratic model is not so robust with respect to the centroid initialization even with a “K-means++” type procedure on this dataset. But this is also the case for all the other testing algorithms. The MBO scheme, which was specifically designed for this dataset [23], does seem to have the highest robustness among all the algorithms.

F. Pavia University, Indian Pines, and Kennedy Space Center Dataset

The Pavia University (9 clusters), Indian Pines (16 clusters), and Kennedy Space Center (12 clusters) datasets are frequently used to test supervised classification algorithms. To save space, we only report the numerical overall accuracies in Table V. As can be seen, all the competing unsupervised algorithms performed poorly on these three datasets. Different clusters were merged and same clusters were splitted in various fashions by all the algorithms, which rendered the numerical accuracies no longer reliable.

The computational run-times of these three datasets are listed in Table IV. Unfortunately, when the number of clusters is increasing, the computational complexity of the quadratic model grows exponentially. The reason is that the number of grid points (δ in Fig. 1) on the unit simplex grows exponentially as the dimension of the simplex increases. Therefore, when the number of clusters is large enough (greater than 10), the stable simplex clustering will become the most time-consuming part of the quadratic model. On these three datasets, we sacrificed the accuracy of the quadratic model by creating a coarser mesh on the unit simplex.

The reason why NLTV, as well as all the other competing unsupervised algorithms, performed poorly on these three datasets is two-fold. First, when the number of classes is too large in a HSI covering a large geographic location, the variation of spectral signatures within the same class cannot be neglected when compared to the difference between the constitutive materials, especially when the endmembers themselves are similar. As a result, the unsupervised algorithms tend to split a ground-truth cluster with large variation in spectral signatures and merge clusters with similar centroids or endmembers. Second, there might exist more distinct materials in the image than reported in the ground truth. Therefore the algorithms might detect those unreported materials because no labeling has been used in these unsupervised algorithms. Thus we can conclude that NLTV,

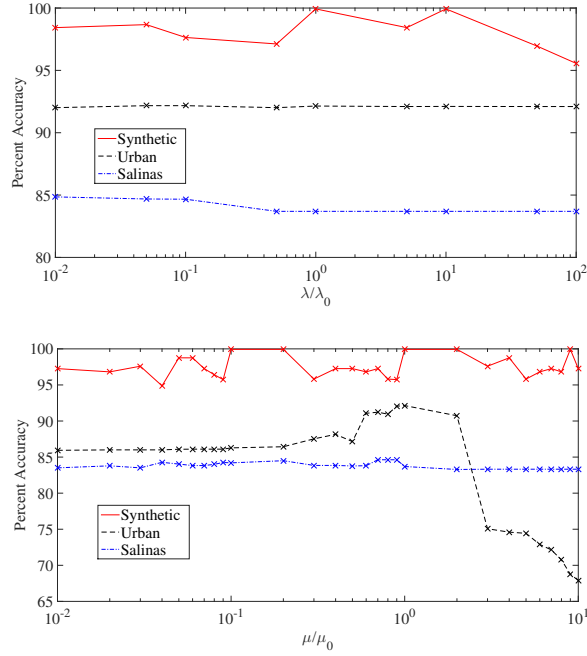


Fig. 9. This figure shows the robustness of the NLTV algorithm with respect to λ and μ . Centroid initialization remains identical as λ and μ are changing. λ_0 and μ_0 are the optimal values specified in Section V-A. The overall accuracies of the Synthetic, Urban, and Salinas-A datasets are displayed.

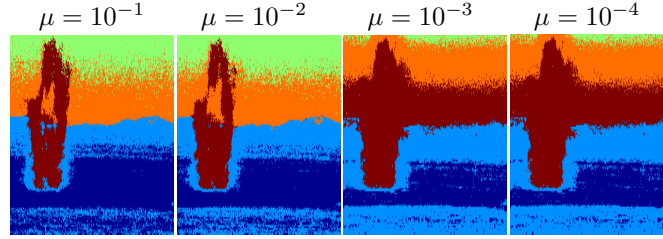


Fig. 10. The sensitivity of the NLTV algorithm with respect to μ in the plume dataset. All the tests used the same centroid initialization (H2NMF).

as well as other unsupervised methods reported in this paper, is not suitable for such images at current stage. Modifying the NLTV algorithm to work for such datasets would be the direction of future work.

G. Sensitivity Analysis over Key Model Parameters

At last, a sensitivity analysis is provided over the parameters λ and μ in the NLTV models. As mentioned in Section V-A, λ and μ are chosen to balance the scale of the regularizing and fidelity terms or the cosine and Euclidean distances. Fig. 9 displays the robustness of the NLTV algorithm on the Synthetic, Urban, and Salinas-A datasets with respect to λ and μ within the variance of two magnitudes. Centroid initialization remains identical as λ and μ are changing. It is clear that the NLTV algorithm is fairly robust with respect to λ on all three datasets. The algorithm is also relatively robust with respect to μ on the Synthetic and Salinas-A datasets. As for the Urban dataset, a significant decay in accuracy can be observed as μ increases. This phenomenon is due to the fact that larger μ causes Euclidean distance to be the dominant one, which is not ideal with the presence of atmospheric interference in the Urban dataset. Smaller μ also leads to lower accuracy in the Urban dataset, which results from the similarity of “road” and “dirt” clusters measured in cosine distance. Overall, a reasonable robustness with respect to the key parameters λ and μ can be concluded on these three tests.

Similar robustness can be observed on other datasets except for the Chemical Plume. Fig. 10 shows the sensitivity of the result with respect to μ . All the centroids are initialized using H2NMF, and vastly different results occurred as μ changes. This could be due to the presence of significant noise.

VI. CONCLUSION

In this paper we present the framework for a nonlocal total variation method for unsupervised HSI classification, which is solved with the primal-dual hybrid gradient algorithm. A linear and a quadratic version of this model are developed; the linear

version updates more quickly and can refine results produced by a centroid extraction algorithm, and the quadratic model with stable simplex clustering method provides a robust means of classifying HSI with randomized pixel initialization.

The algorithm is tested on both a synthetic and seven real-world datasets, with promising results. The proposed NLTV algorithm consistently performed with highest accuracy on synthetic and urbanized datasets such as Urban, Salinas-A, and the San Diego Airport, both producing smoother results with easier visual identification of segmentation, and distinguishing classes of material that other algorithms failed to differentiate. The NLTV algorithm also performed well on anomaly detection scenarios like the Chemical Plume datasets; with proper initialization, it performed on par with the Merriman-Bence-Osher scheme developed specifically for this dataset. However, NLTV, as well as other unsupervised algorithms, failed to achieve satisfactory results on datasets with a relatively large number of clusters. The run-times of the NLTV algorithms are generally comparable to the other methods, and the consistent higher accuracy on different types of datasets suggests that this technique is a more robust and precise means of classifying hyperspectral images with a moderate number of clusters.

APPENDIX

Proof of Theorem 1: Problem (13) is equivalent to:

$$\min_{\sum_{i=1}^k u_i=1} \delta_{\mathbb{R}_+^k}(u) + \frac{1}{2} \|Au - y\|_2^2, \quad (16)$$

where $\mathbb{R}_+^k = \{u \in \mathbb{R}^k : u_i \geq 0\}$ is the nonnegative quadrant of \mathbb{R}^k . The Lagrangian of (16) is:

$$\mathcal{L}(u, \lambda) = \sum_{i=1}^k \left(\frac{1}{2} |a_i u_i - y_i|^2 + \delta_{\mathbb{R}_+}(u_i) + \lambda u_i \right) - \lambda.$$

If u^* is a solution of (16), KKT conditions [43] imply that there exists a λ such that:

$$u^* = \arg \min_u \mathcal{L}(u, \lambda) = \arg \min_{u_i \geq 0} \sum_{i=1}^k \frac{1}{2} a_i^2 \left(u_i + \frac{\lambda - a_i y_i}{a_i^2} \right)^2.$$

Therefore $u_i^* = \max\left(\frac{a_i y_i - \lambda}{a_i^2}, 0\right)$. Meanwhile, the primal feasibility requires:

$$\sum_{i=1}^k u_i^* = \sum_{i=1}^k \max\left(\frac{a_i y_i - \lambda}{a_i^2}, 0\right) = 1.$$

And this proves Theorem 1.

ACKNOWLEDGMENT

The authors would like to thank Zhaoyi Meng and Justin Sunu, for providing and helping with the MBO code.

REFERENCES

- [1] C.-I. Chang, *Hyperspectral imaging: techniques for spectral detection and classification*. Springer Science & Business Media, 2003, vol. 1.
- [2] J. Bioucas-Dias, A. Plaza, N. Dobigeon, M. Parente, Q. Du, P. Gader, and J. Chanussot, "Hyperspectral unmixing overview: Geometrical, statistical, and sparse regression-based approaches," *Selected Topics in Applied Earth Observations and Remote Sensing, IEEE Journal of*, vol. 5, no. 2, pp. 354–379, 2012.
- [3] N. Gillis and S. Vavasis, "Fast and robust recursive algorithms for separable nonnegative matrix factorization," *Pattern Analysis and Machine Intelligence, IEEE Transactions on*, vol. 36, no. 4, pp. 698–714, 2014.
- [4] S. Jia and Y. Qian, "Constrained nonnegative matrix factorization for hyperspectral unmixing," *Geoscience and Remote Sensing, IEEE Transactions on*, vol. 47, no. 1, pp. 161–173, 2009.
- [5] N. Gillis, D. Kuang, and H. Park, "Hierarchical clustering of hyperspectral images using rank-two nonnegative matrix factorization," *Geoscience and Remote Sensing, IEEE Transactions on*, vol. 53, no. 4, pp. 2066–2078, 2015.
- [6] M. Soret, S. L. Bacharach, and I. Buvat, "Partial-volume effect in pet tumor imaging," *Journal of Nuclear Medicine*, vol. 48, no. 6, pp. 932–945, 2007.
- [7] N. Dobigeon, J.-Y. Tournet, C. Richard, J. Bermudez, S. McLaughlin, and A. Hero, "Nonlinear unmixing of hyperspectral images: Models and algorithms," *Signal Processing Magazine, IEEE*, vol. 31, no. 1, pp. 82–94, 2014.
- [8] R. Heylen, M. Parente, and P. Gader, "A review of nonlinear hyperspectral unmixing methods," *Selected Topics in Applied Earth Observations and Remote Sensing, IEEE Journal of*, vol. 7, no. 6, pp. 1844–1868, 2014.
- [9] F. Melgani and L. Bruzzone, "Classification of hyperspectral remote sensing images with support vector machines," *Geoscience and Remote Sensing, IEEE Transactions on*, vol. 42, no. 8, pp. 1778–1790, 2004.
- [10] G. Camps-Valls and L. Bruzzone, "Kernel-based methods for hyperspectral image classification," *Geoscience and Remote Sensing, IEEE Transactions on*, vol. 43, no. 6, pp. 1351–1362, 2005.
- [11] M. Fauvel, J. Benediktsson, J. Chanussot, and J. Sveinsson, "Spectral and spatial classification of hyperspectral data using svms and morphological profiles," *Geoscience and Remote Sensing, IEEE Transactions on*, vol. 46, no. 11, pp. 3804–3814, 2008.
- [12] B. Demir and S. Erturk, "Hyperspectral image classification using relevance vector machines," *Geoscience and Remote Sensing Letters, IEEE*, vol. 4, no. 4, pp. 586–590, 2007.
- [13] G. M. Foody, "Rvmbased multiclass classification of remotely sensed data," *International Journal of Remote Sensing*, vol. 29, no. 6, pp. 1817–1823, 2008.

- [14] F. Mianji and Y. Zhang, "Robust hyperspectral classification using relevance vector machine," *Geoscience and Remote Sensing, IEEE Transactions on*, vol. 49, no. 6, pp. 2100–2112, 2011.
- [15] J. Shi and J. Malik, "Normalized cuts and image segmentation," *IEEE Transactions on Pattern Analysis and Machine Intelligence*, vol. 22, no. 8, pp. 888–905, Aug 2000.
- [16] M. Stoer and F. Wagner, "A simple min-cut algorithm," *J. ACM*, vol. 44, no. 4, pp. 585–591, Jul. 1997. [Online]. Available: <http://doi.acm.org/10.1145/263867.263872>
- [17] A. Szlam and X. Bresson, "A Total Variation-based Graph Clustering Algorithm for Cheeger Ratio Cuts," Tech. Rep. UCLA CAM Report 09-68, 2009.
- [18] X. Bresson and A. D. Szlam, "Total variation, cheeger cuts," in *Proceedings of the 27th International Conference on Machine Learning (ICML-10)*, 2010, pp. 1039–1046.
- [19] A. L. Bertozzi and A. Flenner, "Diffuse interface models on graphs for classification of high dimensional data," *Multiscale Modeling & Simulation*, vol. 10, no. 3, pp. 1090–1118, 2012.
- [20] B. Merriman, J. K. Bence, and S. J. Osher, "Motion of multiple junctions: A level set approach," *Journal of Computational Physics*, vol. 112, no. 2, pp. 334 – 363, 1994.
- [21] C. Garcia-Cardona, E. Merkurjev, A. Bertozzi, A. Flenner, and A. Percus, "Multiclass data segmentation using diffuse interface methods on graphs," *Pattern Analysis and Machine Intelligence, IEEE Transactions on*, vol. 36, no. 8, pp. 1600–1613, 2014.
- [22] "Diffuse interface methods for multiclass segmentation of high-dimensional data," *Applied Mathematics Letters*, vol. 33, pp. 29 – 34, 2014.
- [23] H. Hu, J. Sunu, and A. L. Bertozzi, *Energy Minimization Methods in Computer Vision and Pattern Recognition: 10th International Conference, EMMCVPR 2015, Hong Kong, China, January 13-16, 2015. Proceedings.* Cham: Springer International Publishing, 2015, ch. Multi-class Graph Mumford-Shah Model for Plume Detection Using the MBO scheme, pp. 209–222.
- [24] E. Merkurjev, J. Sunu, and A. Bertozzi, "Graph MBO method for multiclass segmentation of hyperspectral stand-off detection video," in *Image Processing (ICIP), 2014 IEEE International Conference on*, 2014, pp. 689–693.
- [25] "Nonlinear total variation based noise removal algorithms," *Physica D: Nonlinear Phenomena*, vol. 60, no. 14, pp. 259 – 268, 1992.
- [26] T. Chan, S. Esedoglu, F. Park, and A. Yip, "Recent developments in total variation image restoration," *Mathematical Models of Computer Vision*, vol. 17, 2005.
- [27] A. Buades, B. Coll, and J. M. Morel, "A review of image denoising algorithms, with a new one," *Multiscale Modeling & Simulation*, vol. 4, no. 2, pp. 490–530, 2005.
- [28] G. Gilboa and S. Osher, "Nonlocal operators with applications to image processing," *Multiscale Modeling & Simulation*, vol. 7, no. 3, pp. 1005–1028, 2009.
- [29] D. Zosso, G. Tran, and S. J. Osher, "Non-local retinex—a unifying framework and beyond," *SIAM Journal on Imaging Sciences*, vol. 8, no. 2, pp. 787–826, 2015.
- [30] A. Chambolle and T. Pock, "A first-order primal-dual algorithm for convex problems with applications to imaging," *Journal of Mathematical Imaging and Vision*, vol. 40, no. 1, pp. 120–145, 2010.
- [31] J. Zhang, W. Zhu, L. Wang, and N. Jiang, "Evaluation of similarity measure methods for hyperspectral remote sensing data," in *Geoscience and Remote Sensing Symposium (IGARSS), 2012 IEEE International*, 2012, pp. 4138–4141.
- [32] J. H. Friedman, J. L. Bentley, and R. A. Finkel, "An algorithm for finding best matches in logarithmic expected time," *ACM Trans. Math. Softw.*, vol. 3, no. 3, pp. 209–226, Sep. 1977.
- [33] R. A. Brown, "Building a balanced kd tree in $O(kn \log n)$ time," *arXiv preprint arXiv:1410.5420*, 2014.
- [34] M. Muja and D. G. Lowe, "Fast approximate nearest neighbors with automatic algorithm configuration," *VISAPP (1)*, vol. 2, pp. 331–340, 2009.
- [35] M. Zhu and T. Chan, "An efficient primal-dual hybrid gradient algorithm for total variation image restoration," Tech. Rep. UCLA CAM Report 08-34, 2008.
- [36] M. Zhu, S. J. Wright, and T. F. Chan, "Duality-based algorithms for total-variation-regularized image restoration," *Computational Optimization and Applications*, vol. 47, no. 3, pp. 377–400, 2008.
- [37] E. Esser, X. Zhang, and T. F. Chan, "A general framework for a class of first order primal-dual algorithms for convex optimization in imaging science," *SIAM Journal on Imaging Sciences*, vol. 3, no. 4, pp. 1015–1046, 2010.
- [38] D. MacKay, "An example inference task: Clustering," in *Information Theory, Inference and Learning Algorithms.* Cambridge University Press, 2003, ch. 20, pp. 284–292.
- [39] D. Mumford and J. Shah, "Optimal approximations by piecewise smooth functions and associated variational problems," *Communications on pure and applied mathematics*, vol. 42, no. 5, pp. 577–685, 1989.
- [40] J. Kim and H. Park, "Fast nonnegative matrix factorization: An active-set-like method and comparisons," *SIAM Journal on Scientific Computing*, vol. 33, no. 6, pp. 3261–3281, 2011.
- [41] D. Arthur and S. Vassilvitskii, "K-means++: The advantages of careful seeding," in *Proceedings of the Eighteenth Annual ACM-SIAM Symposium on Discrete Algorithms*, ser. SODA '07. Philadelphia, PA, USA: Society for Industrial and Applied Mathematics, 2007, pp. 1027–1035. [Online]. Available: <http://dl.acm.org/citation.cfm?id=1283383.1283494>
- [42] "Structured sparse method for hyperspectral unmixing," *{ISPRS} Journal of Photogrammetry and Remote Sensing*, vol. 88, pp. 101 – 118, 2014.
- [43] S. Boyd and L. Vandenberghe, *Convex optimization.* Cambridge university press, 2004.